Cohesive collisions of particles in liquid media studied by CFD-DEM, video tracking, and Positron Emission Particle Tracking

Nazerke Saparbayeva [a,*], Yu-Fen Chang [a,b], Pawel Kosinski [c], Alex C. Hoffmann [c], Boris V. Balakin [a], Pavel G. Struchalin [a]

[a] Western Norway University of Applied Sciences, Department of Mechanical and Marine Engineering, Bergen, Norway
[b] UiT The Arctic University of Norway, Department of Clinical Medicine, Tromsø, Norway
[c] University of Bergen, Department of Physics and Technology, Bergen, Norway

HIGHLIGHTS

- We consider ice-ice interaction in decane from −15.7 °C to −0.3 °C.
- 4.7 mm particles collide on the inclined ice surface.
- Video & PEPT reveal particle motion.
- CFD-DEM simulations match experimental data.
- Coefficient of restitution peaks around −10.0 °C temperature.

GRAPHICAL ABSTRACT
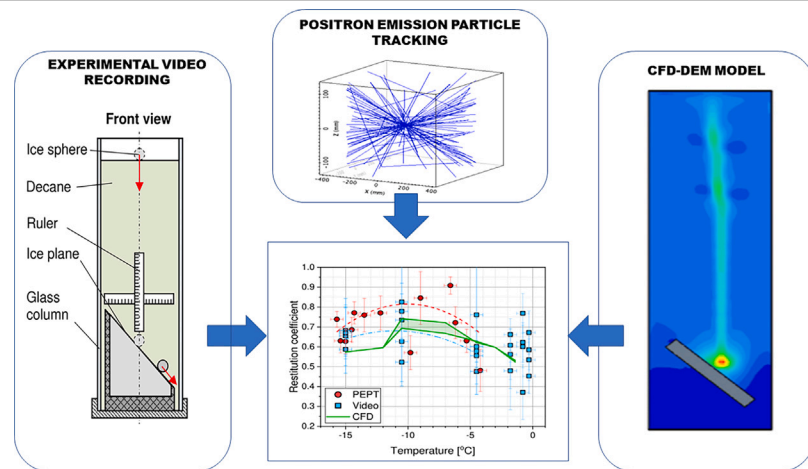
ARTICLE INFO

ABSTRACT

This paper investigates the cohesive collision of ice in an oil phase at temperatures ranging from −15.7 °C to −0.3 °C. The new information on the coefficient of restitution (COR) was obtained using three different velocity measurement methods: high-speed experimental video recording, Positron Emission Particle Tracking (PEPT), and numerical simulations. A new type of PEPT tracer was developed for the experiments. The COR values were in the interval 0.57...0.82, with a maximum at around −10 °C. The CFD-DEM coupled approach was applied to reproduce experiments with an ice particle drop and its collision with an inclined ice surface in a decane. The particle–wall interaction is modeled using commercial software, considering particle cohesion, particle size, and shape. CFD-DEM predicted the COR with an average deviation ~10% from the experimental data. The numerical model's results agree with the experiments, demonstrating that the CFD-DEM method is suitable for describing multiphase cohesive interactions.

---

* Corresponding author.
  E-mail address: nazerke.saparbayeva@hvl.no (N. Saparbayeva).

1. Introduction

The hydraulic transport of ice particles is essential in energy and powder technology as ice slurries are effective coolants and phase change materials [1]. They are also used in the construction sector [2]. A majority of commercial ice slurries use aqueous media to disperse ice [3], which makes them hardly applicable in systems where repeated cycles of melting and solidification are expected since molten particles dissolve in the carrier liquid. To tackle this issue, Matsumoto et al. [4] proposed an oil-based ice slurry capable of turning to emulsion when melting and restoring the suspension of solid particles at temperatures less than 0 °C. Moreover, oil-based slurries are additionally crucial in petroleum technology as ice particles constitute suitable models of gas hydrates [5]. However, once dispersed in an oil phase, ice particles increase their cohesion due to the formation of liquid films at their surface [6]. Pumping an oily slurry through process equipment could become a challenging problem due to the cohesive interactions of ice particles. Their mutual collisions can lead to agglomeration, formation of deposits, and plugging [7].

Several complex phenomena govern the collisions of ice particles in the oil. Attractive cohesion [6] competes with repulsive lubrication forces [8], which are induced by oil and water squeezed out between the colliding surfaces. Mechanical deformation and surface friction of particles during contact dissipate a significant share of their relative energy before the collision [8]. The viscous phase can also influence the process via, e.g., the formation of wakes [9], turbulence [8], thermal convection, and partial slip [10]. In most cases, the shape [11] and the roughness [12] of particles may become crucial.

A simplified approach to characterize particle collisions is to define a coefficient of restitution (COR) [13], i.e., the square root of the ratio of kinetic energy before the collision (E_{k1}) to the kinetic energy after the collision (E_{k2}) [8]. Numerous works are considering the COR of ice particles in a vacuum/gaseous media [14–17]. Dealing with high-impact velocities, they primarily focus on aerospace applications where a particle may crack during the impact. Higa et al. [15] determined the restitution coefficient of ice particles impacting an ice block in the normal direction. The experiments were carried out in vacuum conditions, temperatures above 120 K, and impact velocities from 1 to 10 m/s. The restitution coefficient was based on the linear velocities of the particles determined with a high-speed camera. They found that the restitution coefficient was about 0.9 for velocities below 1 m/s and temperatures below 245 K. Increasing the temperature, the COR progressively reduced to zero at 237 K due to the formation of liquid films at the surface of the ice.

Reitter et al. [17] used a high-speed camera to identify the influence of liquid films and impact angles on the COR for ice particles in the air. They found that COR for normal collisions reduced with the particle Stokes number and the thickness of the film. At the same time, COR for oblique collisions did not alter significantly and was in the interval of 0.8–0.9. Once the so-far-determined ice CORs provide valuable input for the analysis of cohesive slurries, the experiments did not yet account for the influence of the continuous phase. In addition, the used ice particles were not spherical and, depending on an initial orientation, could rotate after the impact. This was not considered in their studies.

Although a limited number of factors influencing the collision of ice particles have been considered, there is a wider knowledge base describing collisions of metals, oxides, and semiconductors [18]. Collisions of wet particles were studied in Antonyuk et al. [19] and Muller et al. [20]. The experimental results demonstrated that COR was dependent on the thickness of the liquid layer covering the particles [20], the viscosity of the ambient media [21], the impact velocity [19], the viscosity and the surface tension of the liquid film, and the size of the colliding particles [19]. Hastie et al. [22] considered COR for objects of irregular shape. The influence of natural [18] and artificial roughness [23] on the COR was considered for different impact velocities. It was found that an increased roughness reduces the COR in the

air. However, as has been recently reported by Krull et al. [24], COR increases with the height of the roughness when the impact happens in liquid media. This is most possibly connected to an altered slip at the tips of the roughness reducing the viscous lubrication [10].

A majority of the conducted COR tests study collisions using high-speed video tracking. Despite the method's accuracy, there are inherent limitations of the technique. To follow a three-dimensional motion of the colliding particles, which is highly relevant for objects of an irregular shape, at least two cameras are required. Direct optical access to the process demands transparency of the studied system, which is hardly compatible with industrial conditions where pressurized, semi-transparent, and often chemically aggressive media are used. A promising alternative experimental technique was proposed by Oesau et al. [11]. The authors studied CORs of colliding particles using the magnetic particle tracking method based on continuous sensing of a dipole magnet. After comparison with standard high-speed video tracking, the method demonstrated surprisingly high accuracy and repeatability of the results. However, the technique requires magnetic tracer particles, which limit the selection of the tested materials. Another limitation is a restriction for using ferromagnetic materials other than tracers. This again reduces the industrial relevance of the studied phenomena and the process equipment that consists of this kind of material.

In light of the discussed limitations, another method involving radioactivity could be more applicable to studying cohesive collisions of ice. Positron emission particle tracking (PEPT) was pioneered at the University of Birmingham [25–28]. This technique allows tracking a particle moving through a process located in the field of view (FOV) of a 3D detector array. PEPT has been an advantageous experimental method for validating and advancing computational fluid dynamics (CFD). The method uses the radioactive decay of a suitable isotope with which a tracer particle is labeled. In this work, Fluorine-18 (^{18}F) gives rise to the emission of a positron that travels a small distance through the medium until it annihilates with an electron, resulting in a back-to-back emission of two photons of 511 keV each. A straight line between two detectors receiving the photon pair of the same annihilation event (i.e., both within a very narrow time window) defines a "line of response" (LOR). This indicates that the annihilation event must have occurred somewhere along this line. From this, algorithms processing many LORs within a short time interval allow the determination of the centroid of the tracer particle. The accuracy of positioning the particle depends mainly on the algorithm and the activity of the tracer particle. Scatter is inherent in the process, and the reasons for this are discussed in Bailey et al. [29] and Chang et al. [30].

PEPT has been utilized to acquire particle motion, settling, and collision in various processes to overcome the limitations of optical methods, such as particle tracking velocimetry (PTV), which works only with an optically transparent system that is unavailable in many cases. PEPT results can therefore reveal the otherwise undetectable information, which can be further compared with the computational models. For instance, Cole et al. [31] analyzed the PEPT tracer particle velocity to deduce information on local foam structure and events, such as coalescence, to study the structure in flotation froths and to improve the CFD models of flotation. In Cole et al. [31], a 70 μm alumina particle labeled with ^{18}F was tracked with a temporal resolution of approximately 7.5 ms during its ascent and descent in a foam column. PEPT was also applied to study the effect of two and three spouts on the flow dynamics in a pseudo-2D fluidized bed, where the depth of the bed was assumed to be sufficiently small to display pseudo-2D behavior [32]. A 3 mm glass bead labeled with ^{18}F was tracked with a temporal resolution of 3–10 ms. A discrete particle model (DPM) that describes the dynamics of the continuous gas phase and particles was used to simulate 3D fluidized beds. A soft sphere approach was used to describe inter-particle collisions. The results of PEPT agreed very well with the instantaneous 2D velocity data obtained by PTV. However, the DPM simulations overpredicted the particle velocity in the annulus

of the fluidized bed. This deviation was likely due to wall effects that are more pronounced in pseudo-2D beds than in 3D systems, which are not treated with sufficient accuracy in DPM. Although PEPT has never been used before for studying adhesive collisions of ice, our group has recently developed a method to produce radioactive ice tracers for this purpose [33].

Based on the discussed experimental studies, we conclude that the coefficient of restitution is not a universal parameter describing the cohesive collisions of ice in oil. The influence of particle surface properties, together with the behavior of the oil phase, alters the coefficient of restitution significantly. Another difficulty comes from the experimental method itself, as the existing techniques are not entirely applicable to the desired process. Theoretical studies of the problem could shed light on those missing phenomena, but there are not many papers published on the matter. Chen et al. [34] performed a CFD study of the collision of a particle with the wall in a viscous medium. In their work, solid particles were modeled as Lagrangian objects using the discrete element method (DEM) to describe the particle–wall interaction [35]. After experimental validation of the model, we consider how the properties of the liquid phase influenced the contact forces during the collision. However, this model did not account for such important factors as lubrication and cohesion. A series of CFD-DEM models devoted to cohesive gas hydrates was published during the last decade [35–37]. In these works, standard collision models built in commercial CFD codes were used to model multiple interactions among particles and with walls. Although some of the models complied with theoretical correlations for agglomeration in cohesive suspension [35], they were applied without considering how realistically they reproduced individual contacts. The lubrication forces were not taken into account there either.

The primary objective of this paper is to provide a detailed physical description of the process of cohesive collisions of ice in an oily dispersed phase. We start with experimental studies of the process at different temperatures and, therefore, different cohesion, using video tracking and PEPT of radioactive ice particles. The next stage is developing a CFD-DEM model accounting for the majority of factors missing in similar studies and validating the model against our experimental data.

2. Methodology

2.1. Experimental system

Cohesive collisions of ice in oil were studied by letting an ice particle impact onto an inclined ice surface immersed in decane (Sigma Aldrich >95%). For this, the ice surface (inclined at the angle of 45°) was placed in a holder within a vertical cylindrical column filled with decane (Figs. 1, 2A). The column was made of a cylindrical pipe (borosilicate glass 3.3) sandwiched between steel (SS 304) flanges with ports equal to the inner diameter of the pipe (42 mm). A plastic plug holding the ice surface was inserted into the lower flange. The resulting distance along the central vertical axis from the upper edge of the column to the ice surface was 260 mm. The total column height was 360 mm, and the diameter was less than 88 mm.

In the PEPT experiments, the column was covered with 17-mm thick EPE foam thermal insulation. During the experiments, the column was fixed on a tripod, and during the video track, a scale was placed near the column. The column was kept at temperatures below the ice melting point and thermally stabilized. An ice particle held in the upper decane layer was released without initial velocity and fell onto the ice surface. The entire settling process was registered to determine the instantaneous velocities of the particle both before and after the collision with the surface. As a final result, based on the particle velocity history and assuming that the particle was nearly-spherical, the ice-in-oil restitution coefficient was determined as (1):

$$\epsilon = \sqrt{\frac{E_{k2}}{E_{k1}}} \sim \sqrt{\frac{v_2^2 + 0.1\omega^2 d^2}{v_1^2}}, \tag{1}$$

where E_{k1}, E_{k2} are the particle kinetic energies and v_1, v_2 are particle linear velocity before and after a collision respectively, ω is a particle angular velocity after collision. The particle kinetic energy of rotation before the collision is absent in Eq. (1) since no significant rotation of the particles was detected *before* the collisions. It is also shown in Section 3.1.

In the laboratory experiments, the particle tracking was done using a high-speed video camera (Sony IMX586 Exmor RS, 48MPx, f/1.79, 240 fps). The focal plane of the lens was aligned with the inclined ice surface. This made it possible to determine the collision moment between the ice particle and the surface.

The ice particles and the inclined ice surface were produced the same way, both for laboratory tests and tests with the PEPT scanner. The ice surface was made by freezing water in a holder at −25 °C. We used tap water for all the experiments, and its chemical composition is presented in the Supplementary materials. After the ice was formed, the surface facing the falling particle was exposed to a warm aluminium plate to form a flat surface at the required angle. The holder edges have the same inclination angle (45°). So, during partial melting, the ice surface is aligned with the edges, achieving the required inclination. After melting, the ice surface was covered with a polished polyethylene plate and placed back in the freezer at the same temperature to freeze the residual water layer between the ice and the plate. This allowed the formation of a flat ice surface. Due to the low adhesion of ice to polyethylene, the plate could be removed without damaging the ice surface.

Ice particles were made of water taken at room temperature. To do this, 80 µl of water were drawn into a standard mechanical pipette (Thermo Scientific Finnpipette EH81075 4500 mechanical pipette 10-100 µl). The pipette was equipped with a standard plastic tip, which was cut to increase the diameter of the tip's outlet hole and to doze out the required volume of water. The pipette tip was immersed in decane at a temperature between −17 and −19 °C. This was done in a supplementary vertical column, as mentioned above, but without the inclined surface. The column had a bottom ball valve to remove the produced ice particles. Ten seconds after the pipette tip was immersed in the cold decane, the water was slowly injected into the decane and formed a single drop. When the drop fell, an ice shell was formed, retaining the shape of a particle close to spherical and holding the rest of the non-crystallized water inside. The crystallization of the remaining water occurred when the drop was at the bottom of the column. Then a new portion of water was taken, and the production process was repeated. Three to five particles were produced at a time. After that, the ball valve at the bottom of the column was opened, and the particles, together with some amount of decane, were extracted into a 400 ml beaker. The beaker was tilted so that the decane with particles fell down along the wall without a substantial impact on the beaker's bottom. At least 60% of the particles from one production procedure remained intact and undamaged. The rest of the particles were destroyed in the process due to high internal mechanical stresses caused by the expansion of water during crystallization inside the pre-formed ice shell. The resulting particles had a shape very close to spherical, with a diameter $d_i = 2r_i = 4.7 \pm 0.3$ mm. Their typical appearance is shown in Fig. 2B.

The produced particles were stored in a decane and were retrieved from it only for use in the main experiment. Prior to this, the temperatures of the decane in the main column and in the beaker were equalized. The temperatures of decane at all the stages of ice particle production and the experiments were controlled by immersed K-type thermocouples (±0.1°C) connected to the RS-42 RS PRO thermometer.

The settling of the particle in a column was analyzed from the recorded video. The linear velocity of a particle was determined from the difference in the coordinates of its geometric center. The coordinates were determined relative to the chosen zero mark on the ruler placed near the ice surface inside the column. For that, the X-Y coordinate system defined in Fig. 2 was used. The processing of the two
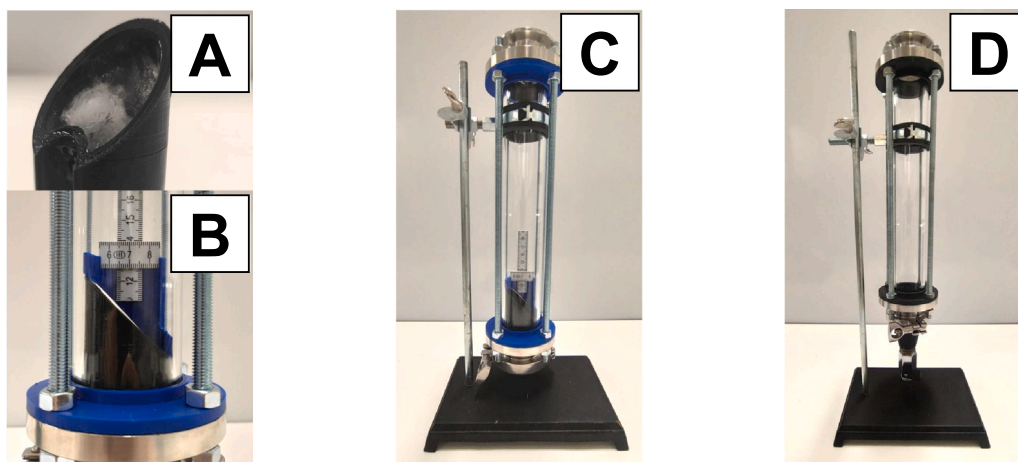
Fig. 1. Photos of the glass columns. The ice surface in a plastic holder (A), its position within a glass column (B), the main column for the drop (C), and the supplementary column for the ice spheres production (D).
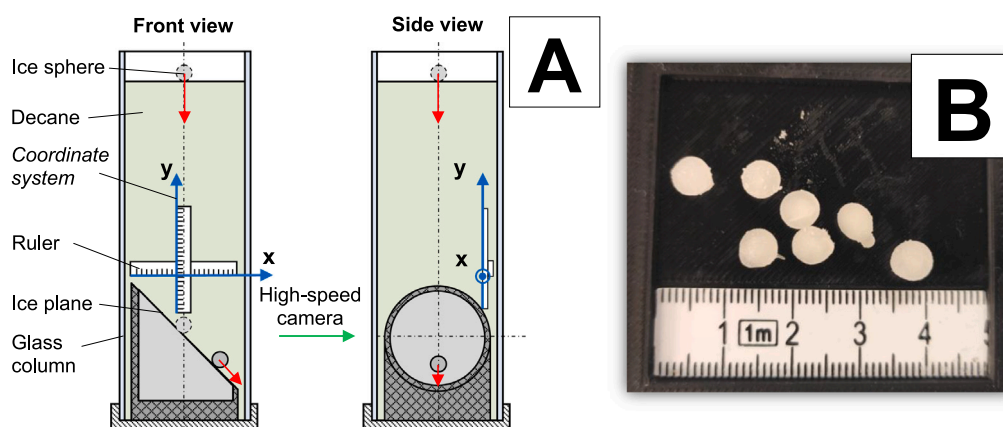

Fig. 2. Experimental set-up (A) and appearance of the ice particles (B).

frames taken at a known time interval τ made it possible to determine the displacement of the particle by a set of initial and final coordinates (x_1, y_1), (x_2, y_2) and calculate its velocity as $v = [(x_2^2 - x_1^2) + (y_2^2 - y_1^2)]^{0.5}/\tau$. The rotational velocity, ω, was determined using the rotational angle α of a line passing through the center of an ice sphere as $\omega = \alpha/\tau$. The time interval was limited to $\tau = 150$ ms, corresponding with the particle's momentum response time [8]. To process the frames and determine the particle coordinates, we used the Grafula 3 software.

We note that our method of velocity determination contains a methodological uncertainty, leading to an underestimation of the instantaneous linear velocity due to its unknown component in the third direction perpendicular to the focal plane of the camera. However, this error did not make a significant contribution. Considering the system to be axisymmetric and assuming the probability of particle motion in all horizontal directions to be the same, the unknown horizontal velocity component could be estimated. The unaccounted particle velocity component underestimated its average absolute value at 0.43% and a maximum value of 2.13%.

The uncertainties of linear velocities in the laboratory tests were determined as $\Delta v = [(\Delta x \cdot \partial v/\partial x)^2 + (\Delta y \cdot \partial v/\partial y)^2 + (\Delta \tau \cdot \partial v/\partial \tau)^2]^{0.5}$ where the uncertainties of the particle coordinates and the time step are $\Delta x, \Delta y = \pm 0.5$ mm and $(\Delta \tau = \pm 4.2$ ms, correspondingly. The uncertainty of the ratio of the linear velocities $VR = v_2/v_1$ is taken as $\Delta VR = [(\Delta v_2 \cdot \partial \Delta VR/\partial v_2)^2 + (\Delta v_1 \cdot \partial \Delta VR/\partial v_1)^2]^{0.5}$.

The COR's measurement uncertainty was defined in the same way from $\Delta \epsilon = [(\Delta v_2 \cdot \partial \epsilon/\partial v_2)^2 + (\Delta v_1 \cdot \partial \epsilon/\partial v_1)^2 + (\Delta d \cdot \partial \epsilon/\partial d)^2 + (\Delta \omega \cdot \partial \epsilon/\partial \omega)^2]^{0.5}$.

2.2. Positron emission particle tracking

Positron emission particle tracking (PEPT) was used to track the 3D movement and velocity of the ice particles. For this purpose, ice particles made of water solution of ^{18}F were located in the ice decane column with a millisecond temporal resolution. The [^{18}F]fluoride was produced from [^{18}O]water targets by the ^{18}O(p,n)^{18}F nuclear reaction, where a neutron (n) and fluorine-18 were produced by the reaction of an accelerated proton (p) with oxygen-18. Each ice particle was made of 80 µl of the ^{18}F aqueous solution by the method described in Section 2.1. The radioactivity per ice particle was around 20–40 MBq.

A detector array surrounding the decaying nuclei is needed to detect the back-to-back photon pairs. In this study, the "Siemens Biograph Vision 600" PET (positron emission tomography) scanner was utilized as the detector array. The cylindrical scanner consists of 80 rings, and each ring consists of 760 LSO (lutetium oxyorthosilicate) crystals in the tangential direction and one crystal in the axial direction. Each crystal is of the dimension 3.2 mm × 3.2 mm × 20 mm. A silicon photomultiplier (SiPM) array couples with a mini block of a 5 × 5 crystal array. For more details on the scanner, refer to [38]. The crystal arrangement creates an axial field of view (FOV) of 263 mm and a radius of 410 mm. 64-bit list-mode data consisting of information on the detector pairs and 1-ms timestamps were acquired. The lines of response (LORs) identified by the detector pairs were then processed to locate the ice particle.

The distance between the positron emission and the annihilation events gives rise to uncertainty in locating the decaying nucleus. This
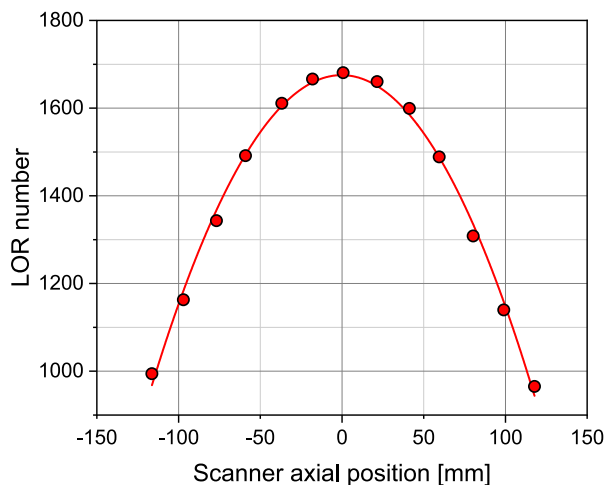
Fig. 3. The number of lines of response (LORs) produced by the ^{22}Na point source placed at different locations along the scanner axial direction as the x–y coordinate is around (1, −176). Each point represents an average of 60 data.

Fig. 4. The 3D standard deviation of 60 positions, as an indication of the positioning accuracy, obtained by processing the LORs of the ^{22}Na point source using the in-house developed algorithm. The point source was placed at different locations along the scanner axial direction as the x–y coordinate is around (1, −176).

distance is related to the initial energy of the positron. For ^{18}F and ^{22}Na, the mean ranges of positrons in water are around 0.6 mm and 0.53 mm, respectively [29,39]. Also, the non-zero momenta of the positron and electron as they annihilate cause deviation from collinearity, which contributes to further uncertainty in the localization of the decaying nucleus. In addition to the above-mentioned sources of uncertainty, other factors, including finite crystal size, depth of interaction in the crystal, electronics properties, and photon deflection due to interaction with other materials, also create false and deviated signals.

To eliminate the influence of erroneous signals and to accurately identify the centroid of the particle, several data processing algorithms have been developed [30,40,41] and refined for the specific detector system and experimental setup. Unlike the projection-based algorithms that are used in general PET reconstruction, in-house developed PEPT algorithms compare the LORs with each other to identify the most probable location of the centroid of the radioactive ice particle. The iterative operation was applied to eliminate false LORs (of which examples are shown in Fig. 5) and increase the position accuracy.

To verify the positioning algorithm used to process the ice particle data and also to check the variations of LOR amount affected by the relative locations in the FOV, a ^{22}Na point source (Eckert & Ziegler) of diameter 250 μm was placed at various axial locations. Since in the actual experiments, the ice particle generates 3000–15000 LORs per positioning interval (4 ms in this study), a period was chosen to obtain around 1700 LORs from the ^{22}Na point source when it was at the FOV center. Then the same data acquisition setting was used as the point source moved to the FOV edge to check how the relative location affects the LOR amount and the positioning accuracy.

As shown in Fig. 3, as the ^{22}Na point source moved away from the FOV center along the scanner axial direction by around 115 mm, the number of LORs was reduced to 60% of the peak number. The resulting positioning accuracy as a function of axial location is plotted in Fig. 4. 3D standard deviations of 60 positions (Fig. 4) were obtained at different locations corresponding to those shown in Fig. 3. Note that in this verification test, ^{22}Na point source was off the center in the plane perpendicular to the scanner axial direction for around 176 mm. More minor standard deviations can be expected if the positron emitter is on the axial axis of the cylindrical scanner. Under this condition, the positioning uncertainties, as indicated by the standard deviations, are below 0.2 mm within around half of the axial FOV range.

Verified with the ^{22}Na point source, the same algorithm was applied to locate the ice particles. Fig. 5(a) shows the LORs of 0.1 ms acquired
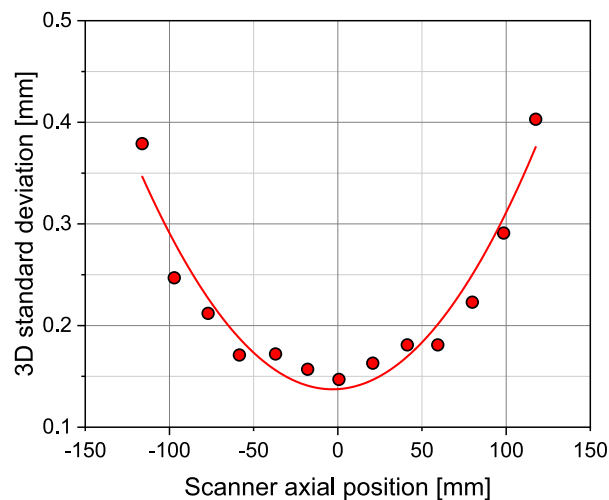
with a stationary ice particle made of 80-μl ^{18}F aqueous solution and the particle was kept still in decane. Fig. 5(b) shows the LORs used for localization after being processed by the iterative algorithm. The 3D standard deviation of 60 positions, each obtained every 4 ms, is 177 μm under the condition of 3015 LORs per 4 ms and the particle at the z-axis center and off $x − y$ center for around 90 mm. Since the LOR amounts in ice collision experiments are usually between 3000 and 15000, and the standard deviation scales with $1/\sqrt{n}$, where n is the number of LORs [40,42], the accuracy in the actual experiments are expected to be better than 177 μm.

The uncertainties of the linear velocities, their ratio, and COR for the PEPT experiments were determined in the same way as for the laboratory tests, using the corresponding uncertainties of the coordinates ($\Delta x = 0.081$ mm, $\Delta y = 0.062$ mm, $\Delta z = 0.145$ mm), and time ($\Delta \tau = 2 \cdot 10^{-12}$ s).

2.3. Model description

CFD-DEM model of a multiphase system was built using the commercial software STAR-CCM+ 2210 17.06.007) [43]. This model was recently validated for settling of Lagrangian particles in viscous fluids [44]. The fluid and solid phases were solved separately in the coupled CFD-DEM method based on the Eulerian–Lagrangian approach. The liquid phase is described by the system of volume-averaged Navier–Stokes equations formulated for a laminar, incompressible, and isothermal fluid [8]:

$$\frac{D\phi}{Dt} = 0, \tag{2}$$

where ϕ is the volume fraction of the liquid, and $D_{...}/Dt$ is the substantial derivative. For the computational cells where Lagrangian particles reside, this parameter is calculated as $1 − V_p/V_c$, where V_p is the total volume of particles and V_c is the volume of the computational cell.

The momentum equation:

$$\rho \frac{D\phi\vec{u}}{Dt} = -\nabla p + \mu \nabla^2 \vec{u} - \vec{f}_{p,\Sigma}, \tag{3}$$

where $\vec{u}$ is the fluid velocity, ρ, and μ are the density and viscosity, respectively, and p is the pressure. The last term of Eq. (3) describes the superposition of inter-phase forces (per unit volume) acting from Lagrangian particles residing in a computational cell. This term is computed scaling the inter-phase forces applied to an individual particle with the number density of particles in the computational cell $n =$
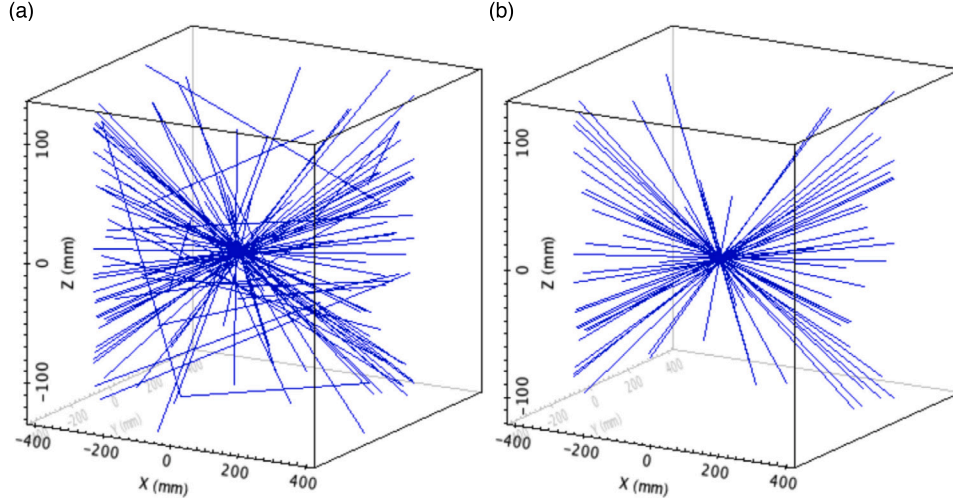
Fig. 5. Lines of response (LORs) of 0.1 ms acquired with a stationary ice particle in decane. The particle was made of 80-μl ^{18}F aqueous solution. The z-axis is the scanner axial axis. (a) Unprocessed LORs. (b) The LORs is used for localization after being processed by the iterative algorithm.

$3\phi/4r_i^3$, where r_i is the radius of the ith particle. We note that Eq. (3) is presented in a general form applicable to a system with multiple particles. However, our system consisted of a single particle.

Newton's second law describes the linear motion of the discrete phase:

$$m_i \frac{\mathrm{d}\vec{v}_i}{\mathrm{d}t} = \vec{f}_{p,i} + \vec{f}_{ls,i} + \vec{f}_{lr,i} + \vec{f}_{b,i} + \vec{f}_{vm,i} + m_i\vec{g} + \sum_{j=1,N_2} \vec{f}_{i,j}, \tag{4}$$

where m_i is particle mass, $\vec{v}_i$ is the particle's velocity, and indices ls, lr, and vm denote the shear, rotational lift forces, and the virtual mass force, respectively, $\vec{f}_{b,i} = \rho/\rho_p m_i\vec{g}$ is the buoyancy force, and ρ_p is the density of the particle. Also, $\vec{f}_{i,j}$ are the forces acting on the ith particle due to contact with N_2 particles and solid boundaries, and $\vec{g}$ is the acceleration due to gravity. The particle rotation is calculated from:

$$\frac{\mathrm{d}}{\mathrm{d}t}(I_i\vec{\omega}_{p,i}) = \sum_{j=1,N_2} \vec{T}_{i,j}, \tag{5}$$

where I_i is the particle moment of inertia, $\vec{\omega}_{p,i}$ is the angular velocity of the particle, and $\vec{T}_{i,j}$ is the total torque of the forces acting on the ith particle due to its contacts.

The drag force acting on the particle is calculated as [8]:

$$\vec{f}_{p,i} = \frac{\pi}{2}r_i^2 c_{D,i}\rho_f(\vec{u} - \vec{v}_i)|\vec{u} - \vec{v}_i|, \tag{6}$$

where $c_{D,i}$ is the drag force coefficient. The drag coefficient is calculated according to the Schiller–Naumann drag coefficient method [8]:

$$c_{D,i} = \begin{cases} (24/\mathrm{Re}_{p,i}) \cdot \left(1 + 0.15\mathrm{Re}_{p,i}^{0.687}\right) & \mathrm{Re}_{p,i} \leq 10^3 \\ 0.44 & \mathrm{Re}_{p,i} > 10^3, \end{cases} \tag{7}$$

where $\mathrm{Re}_{p,i} = 2\rho|\vec{u} - \vec{v}_i|r_i/\mu$ is the particle Reynolds number.

The shear lift force (Saffman force) applies to a particle moving relative to a fluid with a velocity gradient in the fluid orthogonal to the relative motion. The force is given as:

$$\vec{f}_{ls,i} = c_{ls}\rho\pi r_i^3 (\vec{u} - \vec{v}_i) \times \vec{\omega}, \tag{8}$$

where $\vec{\omega} = \nabla \times \vec{u}$ is the curl of the fluid velocity and c_{ls} is the lift coefficient. Sommerfeld's definition of the lift coefficient is used in the model [45]:

$$c_{ls,i} = \frac{4.1126}{\mathrm{Re}_{s,i}^{0.5}} f_i \left(\mathrm{Re}_{p,i}, \mathrm{Re}_{s,i}\right), \tag{9}$$

where $\mathrm{Re}_{s,i} = 4\rho r_i^2|\vec{\omega}|/\mu$ is the Reynolds number for shear flow, and function f is given as:

$$f_i = \begin{cases} \left(1 - 0.3314\beta^{0.5}\right) e^{-0.1\mathrm{Re}_{p,i}} + 0.3314\beta^{0.5} & \mathrm{Re}_{p,i} \leq 40 \\ 0.0524\left(\beta\mathrm{Re}_{p,i}\right)^{0.5} & \mathrm{Re}_{p,i} > 40, \end{cases} \tag{10}$$

$\beta = 0.5\mathrm{Re}_{s,i}/\mathrm{Re}_{p,i}$. The spin lift force (Magnus force) model is applied to calculate the force acting on a spinning particle moving in a fluid [8]:

$$\vec{f}_{lr,i} = \rho\pi r_i^2 c_{lr}|\vec{u} - \vec{v}_i| \frac{\vec{\Omega}_i \times (\vec{u} - \vec{v}_i)}{|\vec{\Omega}_i|}. \tag{11}$$

In the above, $\vec{\Omega}_i$ is the relative angular velocity of the particle to the fluid:

$$\vec{\Omega}_i = 0.5\nabla \times \vec{u} - \vec{\omega}_{p,i}, \tag{12}$$

where $\vec{u}$ is the fluid velocity and $\omega_{p,i}$ is the angular velocity of the particle. The coefficient of rotational lift $c_{lr,i}$ is according to Sommerfeld given as [45]:

$$c_{lr,i} = 0.45 + \left(\frac{\mathrm{Re}_{R,i}}{\mathrm{Re}_{p,i}} - 0.45\right) \exp\left(-0.5684\mathrm{Re}_{R,i}^{0.4}\mathrm{Re}_{p,i}^{0.3}\right), \tag{13}$$

where $\mathrm{Re}_{R,i} = 4\rho r_i^2|\vec{\Omega}_i|/\mu$.

The virtual mass force affects the material particle as it accelerates the surrounding continuous phase:

$$\vec{f}_{vm,i} = c_{vm}\rho V_{p,i} \left(\frac{\mathrm{D}\vec{u}}{\mathrm{D}t} - \frac{\mathrm{d}\vec{v}_i}{\mathrm{d}t}\right), \tag{14}$$

where $c_{vm} = 0.5$ is the virtual mass coefficient.

When the particle comes into contact with its nearest neighbors at the next DEM-time step, the contact forces and torque are activated in Eq. (4),(5). The Hertz–Mindlin contact model with linear cohesion calculates the contact forces in normal, n, and tangential, t, directions relative to the plane of contact between the objects [35]:

$$\vec{f}_{i,j} = F_{i,j}^{(n)}\vec{n} + F_{ij}^{(t)}\vec{t}. \tag{15}$$

The unit vector normal to the contact plane $\vec{n}$ points from the center of colliding ith particle towards the center of the jth particle or the contact zone at the wall.

The normal component of the force then becomes:

$$F_{i,j}^{(n)} = -K^{(n)}\delta^{(n)} - N^{(n)}v_i^{(n)} + F_C, \tag{16}$$

where $\delta^{(n)}$ is the particle-to-wall overlap distance. According to Hertz's theory, $K^{(n)}$ is the "spring's" stiffness in the normal direction employed

in the soft-sphere approach, and it is dependent on $\delta^{(n)}$:

$$K^{(n)} = \frac{4}{3} E_e \sqrt{r_i \delta^{(n)}}, \tag{17}$$

where $E_e = E_i / (1 - v_i^2)$ is the equivalent of Young's modulus, E_i is Young's modulus, and v_i is the Poisson ratio. $N^{(n)}$ is the damping coefficient in the normal direction:

$$N^{(n)} = \sqrt{5 K^{(n)} m_i} \frac{-\ln(\epsilon_{(n)})}{\sqrt{\pi^2 + (\ln \epsilon_{(n)})^2}}, \tag{18}$$

where $\epsilon_{(n)}$ is the coefficient of the particle material restitution in the normal direction. The cohesive force is expressed using Johnson–Kendall–Roberts (JKR) model [46]:

$$F_C = 1.5 r_i W \pi, \tag{19}$$

where W is the work of cohesion. The values for the cohesion work at different experimental temperatures were taken from the work of Yang et al. [6].

The tangential component of the contact force [35]:

$$F_{i,j}^{(t)} = -K^{(t)} \delta^{(t)} - N^{(t)} v_i^{(t)} \tag{20}$$

where

$$\delta^{(t)} = \int_0^{t_c} v_i^{(t)} dt, \tag{21}$$

where t_c is the contact duration [47]:

$$t_c = 2.94 \left(\frac{5\sqrt{2}\pi \rho_p}{4 E_e} \right)^{0.4} r_i v_i^{-1/5}. \tag{22}$$

The stiffness coefficient in the tangential direction:

$$K^{(t)} = 8 G_e \sqrt{r_i \delta^{(t)}}, \tag{23}$$

where $G_e = 0.5 \frac{E_i}{(1 + v_i)}$ is the equivalent shear modulus.

$N^{(t)}$ is the damping coefficient in the tangential direction:

$$N^{(t)} = \sqrt{5 K^{(t)} m_i} \frac{-\ln(\epsilon_{(t)})}{\sqrt{\pi^2 + (\ln \epsilon_{(t)})^2}}, \tag{24}$$

where $\epsilon_{(t)}$ is the particle restitution coefficient in the tangential direction.

In case $|K^{(t)} \delta^{(t)}| > f_s |K^{(n)} \delta^{(n)}|$ the tangential component comes above the sliding limit, a constant $F^{(t)}$ applies as follows [35]:

$$F^{(t)} = f_s |K^{(n)} \delta^{(n)}| \operatorname{sign}\left(\delta^{(t)}\right), \tag{25}$$

where f_s is the Coulomb friction coefficient.

The last aspect of the model is the rolling resistance that gives a resisting torque in Eq. (5):

$$\vec{M}_{i,j} = r_i \mu_r F_{i,j}^{(n)} \frac{-\vec{\omega}_i}{|\vec{\omega}_i|}, \tag{26}$$

where $\mu_r = 2.5 \cdot 10^{-2}$ is the coefficient of rolling resistance.

To account for the lubrication forces in the continuous phase, we used the approach developed by Joseph et al. [48], extrapolating the COR for wet particles from the COR in "dry" conditions:

$$\epsilon_{(n)} = \epsilon_{dry} + \frac{1 + \epsilon_{dry}}{St_0} \ln \frac{x_c}{x_0}, \tag{27}$$

where $\epsilon_{dry} = 0.8$ is the dry restitution coefficient, $St_0 = m_i v_i / 6\pi \mu r_i^2$ is the particle Stokes number before the contact takes place, and $x_c / x_0 \sim 10^{-3}$ is the typical ratio between the inter-particle distance at the point of contact x_c and the terminal position outside the range of the lubrication force x_0 [48]. As in Reitter et al. [17], we set $\epsilon_{dry} = 0.8$, and also assume the coefficient of restitution in the tangential direction was not significantly altered by lubrication, i.e., $\epsilon_{(t)} = \epsilon_{dry}$. The values of the static friction coefficient for ice were taken from recent experiments by

Sukhorukov [49]. They were also linearly interpolated for the temperature interval from our experiments — the obtained values of the static friction coefficient range from 0.57 to 0.71. The physical properties of the ice and the decane were set dependent on the temperature following NIST database [50].

The numerical model was built in the commercial CFD-package STAR-CCM+. The geometry of the computational domain is the same as experimental geometry. The boundary conditions include the pressure boundary at the decane-air interface, and the rest of the surfaces are no-slip walls. As presented in Fig. 6, the computational domain was discretized using 143656 27-mm^3 cubical control volumes to simulate the process of the ice drop falling and the collision with the inclined ice surface. The mesh around the inclined surface is refined to 20% of the mesh base size. A mesh-independence study was performed using mesh sizes twice smaller and 1.5 times larger than the used mesh size. The chosen mesh size resulted in the lowest computational costs, yet the best quantitative agreement with values of particle terminal velocity computed using analytical expressions [8]. A two-grid procedure is used to couple the phases in the vicinity of the boundaries, where the computational cells are smaller than the particle. In this case, the fluid phase was resolved on a larger grid, and then the velocity and the pressure fields were linearly interpolated to the original mesh [51]. In the experiments, the shape of the particles was not ideally spherical. Therefore, composite particles were generated as an assembly of two spheres with the sizes and the offset determined experimentally. They are presented in Fig. 6.

The continuous-phase equations were spatially discretized using central differences. The Euler implicit method was used to advance time with a time step of 10 ms. The governing equations were solved numerically using SIMPLE(Semi Implicit Pressure Linked Equation) with relaxation coefficients: 0.8 velocity, 0.2 pressure, 0.9 volume fraction. A study compared different collision models, including the Hertz–Mindlin and Walton-Brown models [52]. The results showed that both models produced similar outcomes. The minimum time step for the DEM solver was set at 20% of the duration of the Rayleigh wave propagation through the particle [53].

3. Results and discussion

3.1. Experimental trajectories

An example of the particle fall process is shown in Fig. 7 and in the Supplementary video. From the experiments, we conclude that the particle moved vertically enough for most of the drops. Deviations from the vertical trajectory are insignificant, and the moment of collision is well detected. The reason for the horizontal shifts during the falling process is that the particle does not have an ideal spherical shape. Due to the small magnitude, this was challenging to quantify the rotational motion during the particle fall.

A clear rebound does not characterize the collision itself. The particle continues to move along the inclined ice surface without a detachment but starts rolling after the impact. A similar movement of the particle was detected in the PEPT experiments. Fig. 8 shows a typical PEPT-track of the ice particle with a 4 ms time resolution.

The trajectory shows that the particle descended, collided with the inclined ice surface, continued moving along the ice surface, and eventually proceeded further down through a vertical column (Fig. 1A). The particle speed, as shown in Fig. 8(b), downward velocity, and acceleration can be further calculated. As it can be seen in Fig. 8(b), the particle speed decreased abruptly once colliding with the ice surface.

As discussed before, if the particle is not perfectly round, it can be subject to unbalanced lateral forces while settling in decane. This results in lateral movements as can be seen in the figures. It is observed that the particle experienced a speed drop and a speed recovery around the collision event, which is likely an indication of a rebound. In the PEPT experiments, the rebound velocity was identified at the time when the descending speed reached a local minimum (minimal downward motion). Also, the velocity before the collision was identified just before this local minimum descending.
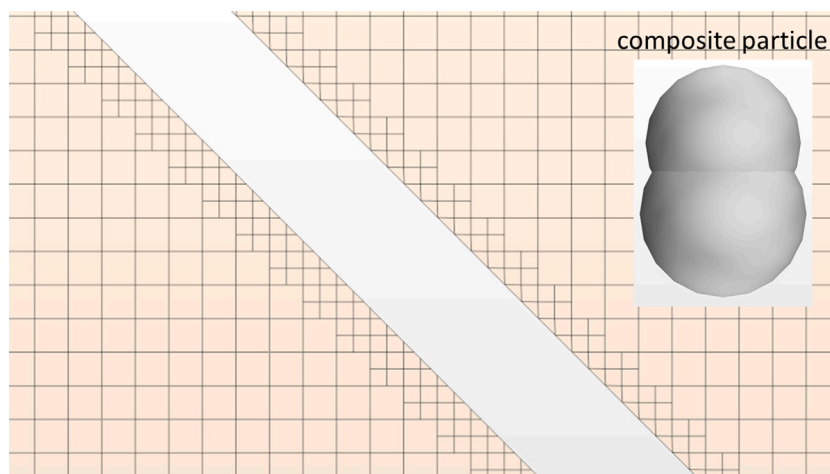
Fig. 6. Computational grid at the inclined surface and particle geometry.

Fig. 7. Particle trajectory during experiments obtained combining video snapshots.

3.2. CFD-DEM

The numerical analysis was carried out for a temperature interval from −15 °C to −1.4 °C. For illustration, Fig. 9 shows the particle velocity as a function of time at −4.5 °C. As can be seen from the figure, the first time interval (1) corresponds to the initial particle's downward motion when the velocity of the particle accelerates with a simultaneous increase in the drag force. After the interval (1), the terminal velocity was reached. According to the simulation, the average value of this velocity was 12 cm/s. The time interval when the particle moves with this constant speed is denoted as (2) in the figure. At the next stage (3), when the ice particle collides with the inclined ice surface, the velocity drops to about 7 cm/s due to mechanical deformation (including lubrication) and cohesion. After collision (4), the particle accelerates again due to gravity up to a value close to the terminal velocity. At the last stage (5), the velocity drops sharply as the particle reaches the bottom of the column and rebounds slightly, changing the velocity magnitude. Fig. 9 also illustrates how the temporal change of the total contact forces during motion along the ice surface. As follows from the figure, the contact forces are negative at the first collision of the particle with the wall due to the deformation of the materials. The overlap reduces from an initial value of 16 μm to ∼7 μm during the next rounds of particle deformation. The magnitude of the forces is about 3 times higher than the cohesive force, which is ∼1 mN in this case. The positive peaks appear at the moments of system reloading after the first repulsion when the particle is directed back towards the surface under the simultaneous action of gravity and cohesion. Fig. 10 demonstrates an imprint of the particle's trajectory onto the velocity field in the liquid. According to the figure, the particle's trajectory is not strictly vertical, which was also observed in the experiments. Due to the non-spherical shape, the particle scours, and then lift forces come into action. As expected, the velocity of the liquid phase reaches a maximum around the moving particle. The average velocity values are observed along the trajectory of the particle, and the lowest values correspond to the remaining regions. The velocity in the area below an inclined plane is almost zero before an ice particle collides with it, but it increases slightly after the particle–wall collision.

3.3. COR and model validation

The video experiments were carried out in the temperature range from −15 °C to −0.3 °C, while the temperature for the PEPT experiments varied in the range from −15.7 °C to −4.2 °C. The summary of these studies and their comparison with CFD simulation are discussed below. We note that the repeatability of experimental results for temperatures above −2 °C was complex due to difficulties in thermal stabilization. This was the primary source of scattering of the experimental data. However, as it will be shown below, the reliability of the obtained data is confirmed by their agreement in the measurements done by different methods.

Fig. 11 presents the linear velocities of the particles before and after the collision with the ice surface. We conclude that the velocities obtained by the different methods are in good agreement with each other. Taking the results from the video experiments as a reference, the average/maximum deviations of the PEPT experiments and the simulation results are 6.6/28.8% and 8.8/12.9% for the velocities before the collision. They are 23.8/46.4% and 12.8/16.7% for the velocities after the collision, respectively.

The effect of the temperature on the particle velocities before and after the collision is different. Considering the results of simulation and laboratory tests first, we observe the particle velocity *before* the collision slightly increases with the temperature. In contrast, the particle velocity *after* the collision tends to have a maximum value at a temperature of −9.9 °C (video) and −12 °C (CFD).

The velocity *before* the collision increases with the temperature as the viscosity of decane reduces [50]. At the same time, the particle velocity *after* impact increases too, but only up to a specific temperature. This is probably due to the reduction of the ice friction coefficient with temperature followed by an increased cohesion of ice [6,7] coming
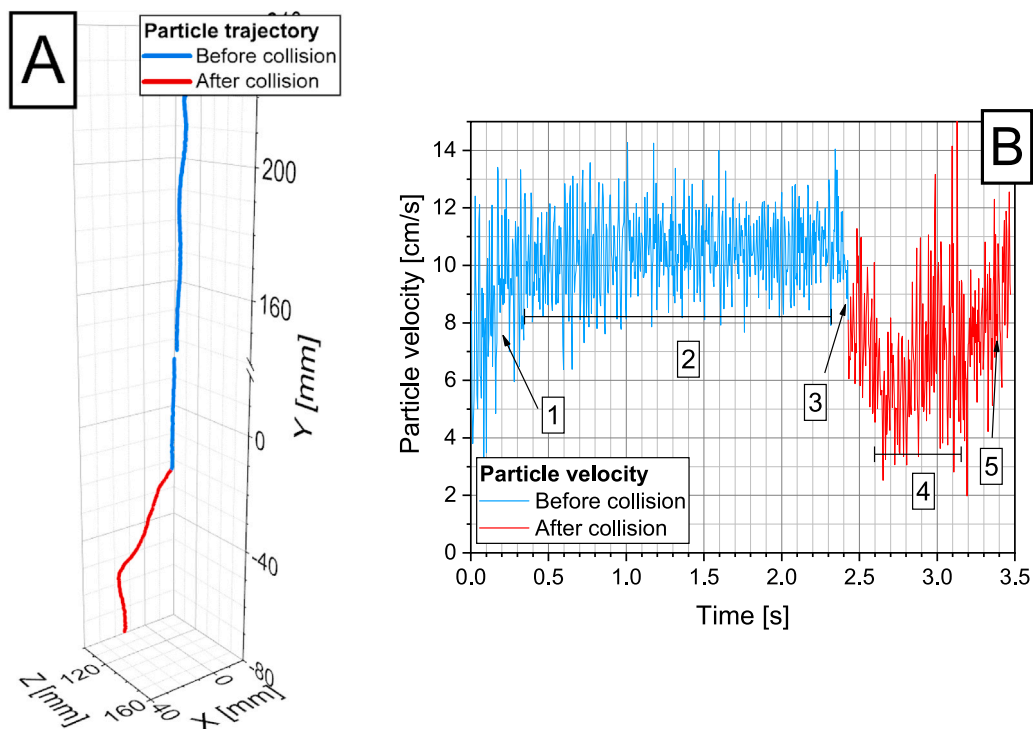
Fig. 8. Particle track in decane obtained by PEPT with a temporal resolution of 4 ms (A), and particle velocity history (B). The particle is released (1) and sedimented in decane (2), collided with the inclined ice surface (3), continued moving along the ice surface (4), and eventually fell further down through a vertical tunnel (5).
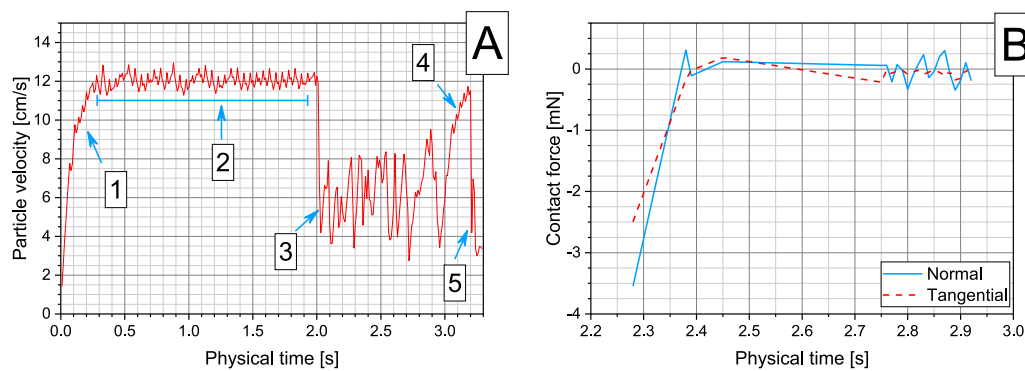

Fig. 9. Temporal changes in particle velocity (A) and contact forces (B) at −4.5 °C obtained using a CFD-DEM model, depicting the particle's movement as it was released (1), settled in decane (2), collided with the inclined ice surface (3), slid along the ice surface (4), and ultimately dropped down a vertical tunnel (5).
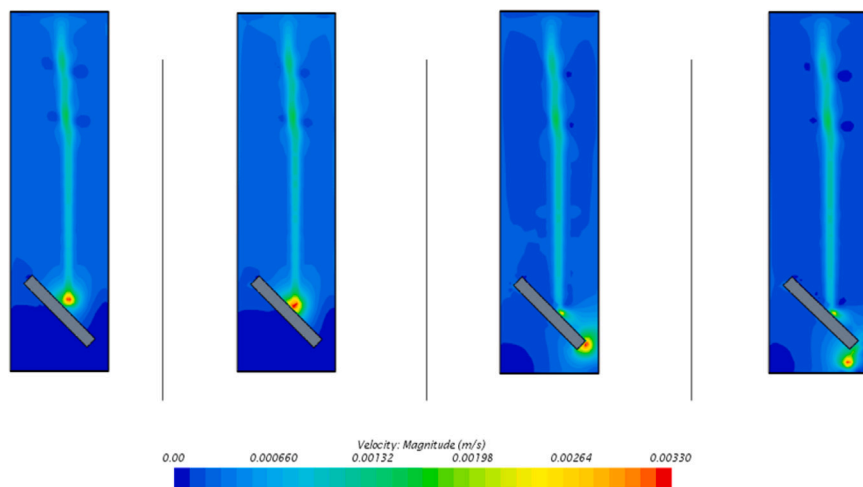

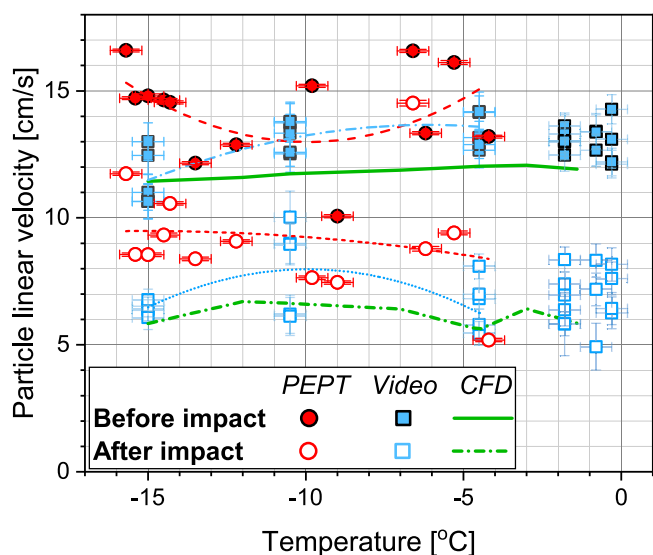**Fig. 10.** Velocity distribution of the fluid phase at four different moments of the time at −4.5 °C.

Fig. 11. Particle linear velocities as a function of temperature. Polynomial approximations of experimental results are given for reference.
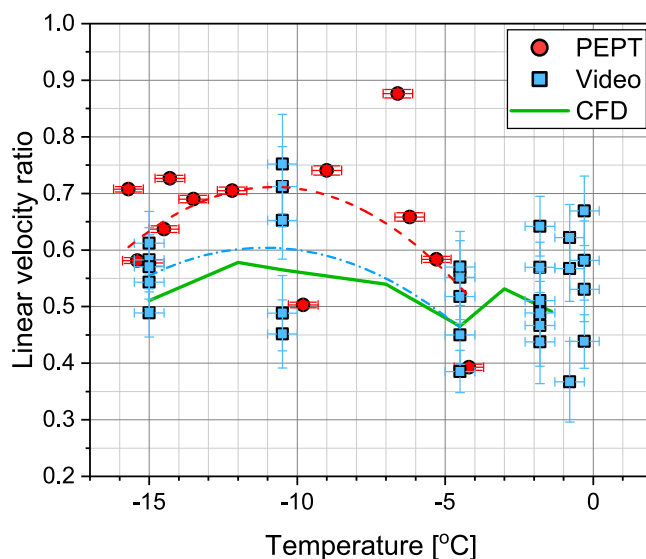

Fig. 12. Velocity ratio as a function of temperature. Polynomial approximations of experimental results are given for reference.

into action and dominating all other effects, continuously reducing the velocity when increasing the temperature.

A slightly different behavior of particle velocities was found in PEPT experiments. Here the velocity *before* the collision has a *minimum* value at around −9.9 °C, while the velocity *after* the collision constantly decreases within the entire studied temperature range. We attribute these results to a broader spread of particle velocity caused by the lower accuracy of the PEPT experiments because of the more complicated experimental procedure. We also note that the thermal stabilization was imperfect in the PEPT experiments as the portal of the scanner is subjected to automatic ventilation. Therefore, thermal convection of the decane was possible there.

Despite that, the linear velocity ratio (VR = v_2/v_1) for all of the methods is similar (Fig. 12). Taking the fitted values of VR from the video experiments as a reference, the average deviation of the CFD and PEPT is 4.2%, and 16.9%, respectively, and the maximum deviations are 8.1% and 18.1%, respectively. All the methods show the VR has a local maximum which is 0.711 at −10.8 °C (PEPT), 0.605 at −11.1 °C (video), and 0.578 at −12 °C (CFD). The appearance of the VR maximum is a consequence of linear velocity behavior. Ice cohesion, friction, and viscosity are the primary factors affecting the maximum linear velocity ratio. These factors affect particle motion differently and contribute to the overall system behavior. Due to increasing ice cohesion in decane when the temperature increases [6,7], the particle impact becomes less elastic. In contrast, decreasing ice friction and viscosity of decane with increasing temperature causes the drag and shear forces acting on the particle to decrease, leading to a permanent increase in particle velocity before impact. The observed maximum VR results from a balance between the increased ice cohesion and decreased friction, which simultaneously progress with the increased temperature. Below the extremum, the friction is reduced with temperature while the cohesion is still low. Therefore, VR increases. Increasing the temperature above the extremum makes the cohesion effect more dominant, decreasing the linear velocity ratio.

The influence of ice cohesion forces is also seen from the angular velocities of the particle after the impact (Fig. 13). Here, the laboratory experiments showed the angular velocity has a maximum at the temperature of −9.6 °C. Then, the angular velocity reduces with the increase in temperature. The simulation showed a slightly higher temperature for the maximum angular velocity point, around −4.5 °C. Nevertheless, in general, the data are in good agreement with each other.
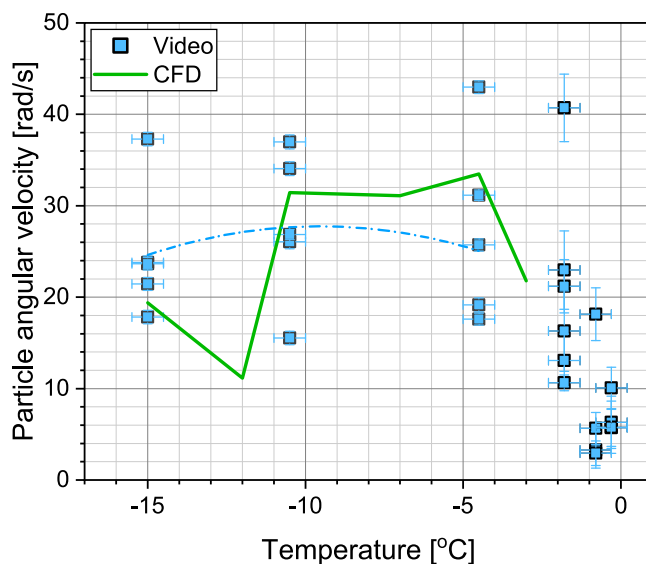

Fig. 13. Angular particle velocity as a function of temperature. Polynomial approximations of experimental results are given for reference.

The average and maximum deviation of simulation from the video experiments are 28.5% and 58.8%. This significant spread is, however, expected since the shape of the particles is a non-ideal sphere. Due to that, the variations of angular velocities appear if a particle touches the ice plane with a more or less flat section of its surface. We note that no information on the particle's angular velocity is available from our PEPT method.

The coefficient of restitution of ice in decane was determined using linear and angular velocities as a square root of the ratio of particle kinetic energies before and after an impact, according to Eq. (1). Fig. 14 presents these calculations. It should be noted that since the particle rotation could not be quantified in the PEPT experiments, we took the fitted values of particle angular velocity from the video experiments. To illustrate how cohesion influences the COR, in this figure, we show the CFD results from two different simulation series: one produced using the median cohesive force from Yang et al. [6] and those with 95%-based values. From Fig. 14, we conclude that there is a good agreement
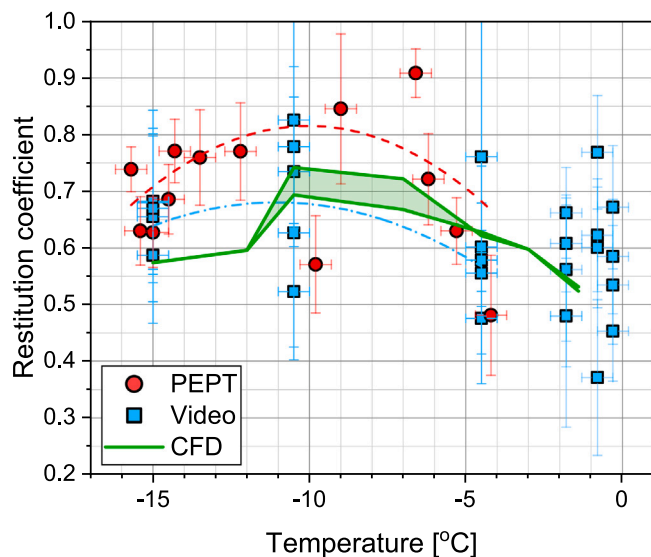
Fig. 14. Coefficient of restitution of ice in decane. Polynomial approximations of experimental results are given for reference.

between the video experiments and CFD simulation. The average and maximum deviation of simulation from lab tests are 9.4% and 12.1%. Deviation of the PEPT experiments is higher and equals to an average of 19.0% and a maximum of 21.7%. For all three methods, a temperature of maximum COR can be found at −11.0 °C (video), −10.5 °C (CFD), and −10.0 °C (PEPT). These temperatures agree with each other, corresponding to the maximal values of COR 0.680 (video), 0.742/0.693 (CFD, median cohesive force/95%-based values), and 0.816 (PEPT). The temperature trend of COR is similar for all three methods. With increasing temperature, the COR first increases until the temperature of maximum COR. Then, the COR decreases, reaching a similar or slightly lower value at −4.2 °C than at the lowest considered temperatures. The minimum obtained values of the COR are 0.567 (video), 0.574 (CFD), and 0.682 (PEPT).

4. Conclusions

This paper provides new data on the restitution coefficient of ice in decane in the temperature range from −15.7 °C to −0.3 °C. The restitution coefficient was proportional to the ratio of kinetic energies of a falling particle in decane before and after its collision with an inclined ice surface. Particle velocity measurements were carried out using the Positron-Emission Particle Tracking technique (PEPT) and high-speed video recording. Both methods provided similar data on the linear velocities, their ratios, and the restitution coefficient (COR). However, the COR has average and maximum deviations between PEPT experiments and the camera-recorded experiments of 19.0% and 21.7%. The reasons for that are thought to be the more complicated procedure of the PEPT experiments compared to the laboratory tests and the impossibility of determining the angular velocity of a particle after its collision with the ice surface.

The coefficient of restitution has a maximum value at −10.0/−11.0 °C (PEPT/video). This value is 0.816/0.680, while the minimum values within the temperature range of −15.7...−4.2 °C are 0.682/0.567 (PEPT/video). The increasing restitution coefficient is due to the decreasing viscosity of the decane, and the decreasing values are due to cohesion.

The experiments were reproduced using CFD-DEM, considering the cohesion, temperature-dependent properties of the materials, and shape of the particles. The restitution coefficient obtained in the simulations deviates from the video-recorded experiments with an average discrepancy of 9.4%. The simulation reproduced the actual particle tracks well,

giving particle velocities very close to the actual ones. The average deviations of the simulated particle linear and angular velocities from the experimental values were about 10.8%. Based on the successful validation of the model with experimental results, we conclude that the cohesive CFD-DEM model implemented in Star-CCM+ is sufficiently accurate.

CRediT authorship contribution statement

Nazerke Saparbayeva: Investigation, Writing – review & editing. **Yu-Fen Chang:** Investigation, Writing – review & editing. **Pawel Kosinski:** Supervision. **Alex C. Hoffmann:** Supervision. **Boris V. Balakin:** Supervision, Investigation, Writing – review & editing. **Pavel G. Struchalin:** Investigation, Writing – review & editing.

Declaration of competing interest

The authors declare the following financial interests/personal relationships which may be considered as potential competing interests: Boris Balakin reports financial support was provided by Research Council of Norway.

Data availability

Data will be made available on request.

Acknowledgments

Appendix A. Supplementary data

Supplementary material related to this article can be found online at https://doi.org/10.1016/j.powtec.2023.118660.

References

[1] M. Kauffeld, S. Gund, Ice slurry–History, current technologies and future developments, Int. J. Refrig. 99 (2019) 264–271.

[2] L. Liu, Z. Fang, M. Wang, C. Qi, Y. Zhao, C. Huan, Experimental and numerical study on rheological properties of ice-containing cement paste backfill slurry, Powder Technol. 370 (2020) 206–214.

[3] M. Kauffeld, M. Kawaji, P.W. Egolf, Handbook on Ice Slurries, Vol. 359, International Institute of Refrigeration, Paris, 2005.

[4] K. Matsumoto, M. Okada, T. Kawagoe, C. Kang, Ice storage system with water–oil mixture: formation of suspension with high IPF, Int. J. Refrig. 23 (5) (2000) 336–344.

[5] P.J. Rensing, M.W. Liberatore, A.K. Sum, C.A. Koh, E.D. Sloan, Viscosity and yield stresses of ice slurries formed in water-in-oil emulsions, J. Non-Newton. Fluid Mech. 166 (14–15) (2011) 859–866.

[6] S.-o. Yang, D.M. Kleehammer, Z. Huo, E. Sloan, K.T. Miller, Temperature dependence of particle–particle adherence forces in ice and clathrate hydrates, J. Colloid Interface Sci. 277 (2) (2004) 335–341, http://dx.doi.org/10.1016/j.jcis.2004.04.049.

[7] P.G. Struchalin, V.H. Øye, P. Kosinski, A.C. Hoffmann, B.V. Balakin, Flow loop study of a cold and cohesive slurry. pressure drop and formation of plugs, Fuel 332 (2023) 126061.

[8] C. Crowe, M. Sommerfeld, Y. Tsuji, Multiphase Flow with Droplets and Particles, CRC Press, 1998.

[9] A. Hooshanginejad, A. Baskota, S. Jung, Backflipping motion of air bubbles colliding with a tilted wall, 2022, arXiv preprint arXiv:2208.14486.

[10] O.I. Vinogradova, G.E. Yakubov, Surface roughness and hydrodynamic boundary conditions, Phys. Rev. E 73 (4) (2006) 045302.

[11] T. Oesau, P. Grohn, S. Pietsch-Braune, S. Antonyuk, S. Heinrich, Novel approach for measurement of restitution coefficient by magnetic particle tracking, Adv. Powder Technol. 33 (1) (2022) 103362.

[12] B.V. Balakin, S. Alyaev, A.C. Hoffmann, P. Kosinski, Micromechanics of agglomeration forced by the capillary bridge: The restitution of momentum, AIChE J. 59 (11) (2013) 4045–4057.

[13] T. Eidevåg, E.S. Thomson, S. Sollén, J. Casselgren, A. Rasmuson, Collisional damping of spherical ice particles, Powder Technol. 383 (2021) 318–327.

[14] F.G. Bridges, A. Hatzes, D. Lin, Structure, stability and evolution of Saturn's rings, Nature 309 (5966) (1984) 333–335.

[15] M. Higa, M. Arakawa, N. Maeno, Measurements of restitution coefficients of ice at low temperatures, Planet. Space Sci. 44 (9) (1996) 917–925.

[16] T. Hauk, E. Bonaccurso, I. Roisman, C. Tropea, Ice crystal impact onto a dry solid wall. Particle fragmentation, Proc. R. Soc. A 471 (2181) (2015) 20150399.

[17] L.M. Reitter, A. Mayrhofer, C. Tropea, J. Hussong, Experimental investigation of normal and oblique impact of ice particles onto a wetted wall, in: AIAA AVIATION 2022 Forum, 2022, p. 3533.

[18] S. Antonyuk, S. Heinrich, J. Tomas, N.G. Deen, M.S. Van Buijtenen, J. Kuipers, Energy absorption during compression and impact of dry elastic-plastic spherical granules, Granul. Matter 12 (1) (2010) 15–47.

[19] S. Antonyuk, S. Heinrich, N. Deen, H. Kuipers, Influence of liquid layers on energy absorption during particle impact, Particuology 7 (4) (2009) 245–259.

[20] T. Müller, K. Huang, Influence of the liquid film thickness on the coefficient of restitution for wet particles, Phys. Rev. E 93 (4) (2016) 042904.

[21] P. Gondret, M. Lance, L. Petit, Bouncing motion of spherical particles in fluids, Phys. Fluids 14 (2) (2002) 643–652.

[22] D. Hastie, Experimental measurement of the coefficient of restitution of irregular shaped particles impacting on horizontal surfaces, Chem. Eng. Sci. 101 (2013) 828–836.

[23] F. Krull, R. Hesse, P. Breuninger, S. Antonyuk, Impact behaviour of microparticles with microstructured surfaces: Experimental study and DEM simulation, Chem. Eng. Res. Des. 135 (2018) 175–184.

[24] F. Krull, J. Mathy, P. Breuninger, S. Antonyuk, Influence of the surface roughness on the collision behavior of fine particles in ambient fluids, Powder Technol. 392 (2021) 58–68.

[25] Y. Fangary, M. Barigou, J. Seville, D. Parker, Fluid trajectories in a stirred vessel of non-newtonian liquid using positron emission particle tracking, Chem. Eng. Sci. 55 (24) (2000) 5969–5979.

[26] F. Snieders, A. Hoffmann, D. Cheesman, J. Yates, M. Stein, J. Seville, The dynamics of large particles in a four-compartment interconnected fluidized bed, Powder Technol. 101 (3) (1999) 229–239.

[27] B. Hoomans, J. Kuipers, M.M. Salleh, M. Stein, J. Seville, Experimental validation of granular dynamics simulations of gas-fluidised beds with homogenous in-flow conditions using positron emission particle tracking, Powder Technol. 116 (2–3) (2001) 166–177.

[28] D. Parker, A. Dijkstra, T. Martin, J. Seville, Positron emission particle tracking studies of spherical particle motion in rotating drums, Chem. Eng. Sci. 52 (13) (1997) 2011–2022.

[29] D.L. Bailey, D.W. Townsend, P.E. Valk, M.N. Maisey, Positron Emission Tomography: Basic Sciences, Springer London, 2006.

[30] Y.F. Chang, T.C.H. Adamsen, A.C. Hoffmann, Using a PET camera to track individual phases in process equipment with high temporal and spatial resolutions: Algorithm development, in: 2012 IEEE International Instrumentation and Measurement Technology Conference Proceedings, 2012, pp. 2326–2330, http://dx.doi.org/10.1109/I2MTC.2012.6229306.

[31] K. Cole, K. Waters, X. Fan, S. Neethling, J. Cilliers, Combining Positron Emission Particle Tracking and image analysis to interpret particle motion in froths, Miner. Eng. 23 (11–13) (2010) 1036–1044.

[32] M.S. Van Buijtenen, W.-J. Van Dijk, N.G. Deen, J. Kuipers, T. Leadbeater, D. Parker, Numerical and experimental study on multiple-spout fluidized beds, Chem. Eng. Sci. 66 (11) (2011) 2368–2376.

[33] Y.-F. Chang, B.V. Balakin, Novel bio-compatible tracers for positron emission particle tracking, in: J. Phys.: Conf. Ser., 1689, (1) IOP Publishing, 2020, 012019.

[34] L. Chen, Y. Wang, J.J. Klemeš, J. Wang, W. Tao, Study on collision between single coarse particle and wall in viscous media using CFD–DEM, Eur. J. Mech. B Fluids (2022).

[35] A.S. Hellestø, M. Ghaffari, B.V. Balakin, A.C. Hoffmann, A parametric study of cohesive particle agglomeration in a shear flow—Numerical simulations by the discrete element method, J. Dispers. Sci. Technol. 38 (5) (2017) 611–620.

[36] X. Duan, B. Shi, J. Wang, S. Song, H. Liu, X. Li, Y. Chen, Q. Liao, J. Gong, S. Chen, et al., Simulation of the hydrate blockage process in a water-dominated system via the CFD-dem method, J. Nat. Gas Sci. Eng. 96 (2021) 104241.

[37] Y. Li, J. Zhao, B. Shi, J. Gong, Q. Li, et al., Simulation of the effect of hydrate adhesion properties on flow safety in solid fluidization exploitation, Petroleum (2022).

[38] J. Van Sluis, J. De Jong, J. Schaar, W. Noordzij, P. Van Snick, R. Dierckx, R. Borra, A. Willemsen, R. Boellaard, Performance characteristics of the digital biograph vision PET/CT system, J. Nucl. Med. 60 (7) (2019) 1031–1036.

[39] L. Jødal, C. Le Loirec, C. Champion, Positron range in PET imaging: non-conventional isotopes, Phys. Med. Biol. 59 (23) (2014) 7419–7434.

[40] Y.-F. Chang, C. Ilea, Ø. Aasen, A. Hoffmann, Particle flow in a hydrocyclone investigated by positron emission particle tracking, Chem. Eng. Sci. 66 (18) (2011) 4203–4211.

[41] Y.-F. Chang, A.C. Hoffmann, A Lagrangian study of liquid flow in a reverse-flow hydrocyclone using positron emission particle tracking, Exp. Fluids 56 (1) (2015) 4, http://dx.doi.org/10.1007/s00348-014-1875-5.

[42] C. Wiggins, R. Santos, A. Ruggles, A feature point identification method for positron emission particle tracking with multiple tracers, Nucl. Instrum. Methods Phys. Res. A 843 (2017) 22–28.

[43] P. Siemens, STAR-CCM+ User Guide Version 2210, Siemens PLM Software Inc., Munich, Germany, 2022.

[44] J.J. Casarin, A.T. Franco, E.M. Germer, R.G. Pivovarski, Numerical simulation of the particle settling in a Bingham fluid using the two-way coupling CFD-DEM scheme, J. Theoret. Appl. Mech. 60 (2022).

[45] M. Sommerfeld, et al., Theoretical and Experimental Modelling of Particulate Flows, in: Lecture Series, vol. 6 (2000) 3–7.

[46] K.L. Johnson, K.L. Johnson, Contact Mechanics, Cambridge University Press, 1987.

[47] S. Timoshenko, J.N. Goodier, Theory of Elasticity: By S. Timoshenko and JN Goodier, McGraw-Hill, 1951.

[48] G. Joseph, R. Zenit, M. Hunt, A. Rosenwinkel, Particle–wall collisions in a viscous fluid, J. Fluid Mech. 433 (2001) 329–346.

[49] S. Sukhorukov, Ice-Ice and Ice-Steel Friction in Field and in Laboratory, Norges teknisk-naturvitenskapelige universitet, Fakultet for ..., 2013.

[50] Thermophysical properties of decane. NIST chemistry webbook, 2022, https://webbook.nist.gov/cgi/fluid.cgi?ID=C124185&Action=Page. (Accessed 24 November 2022).

[51] Siemens Digital Industries Software, Simcenter STAR-CCM+ user guide v. 2020.1, 2020, Siemens.

[52] O.R. Walton, Numerical simulation of inclined chute flows of monodisperse, inelastic, frictional spheres, Mech. Mater. 16 (1–2) (1993) 239–247.

[53] P.C. Vinh, R. Ogden, On formulas for the Rayleigh wave speed, Wave Motion 39 (3) (2004) 191–197.